Applied Surface Science 467–468 (2019) 1134–1139

Contents lists available at ScienceDirect

Applied Surface Science

journal homepage: www.elsevier.com/locate/apsusc

Short Communication

Effects of interfaces on the helium bubble formation and radiation hardening of an austenitic stainless steel achieved by additive manufacturing

Xiangyu Sun[a], Feida Chen[a], Hai Huang[a], Jiwei Lin[a], Xiaobin Tang[a,b,*]

[a] Department of Nuclear Science & Engineering, Nanjing University of Aeronautics and Astronautics, Nanjing 211106, China
[b] Jiangsu Engineering Laboratory of Nuclear Energy Equipment Materials, Nanjing 211106, China

ARTICLE INFO

Keywords:
Selective laser melting
Stainless steel
Interface
Helium bubbles
Radiation hardening

ABSTRACT

Selective laser melting (SLM) provides a novel path to fabricate austenitic stainless steels used in the nuclear reactors. Meanwhile, obvious differences in the microstructures of materials present between SLM and conventional process, which causes a discrepancy in the helium (He) tolerance. In present work, an austenitic stainless steel (type 316L) manufactured through SLM was irradiated by He ions at 450 °C with the concentration approximately 0.8% and then characterized via multiple methods. Results showed the special microstructure containing cellular sub-grains and nano-oxide inclusions, which formed owing to the SLM process, still distributed in post-irradiated samples. A decrease in the bubbles density, swelling rate, and hardness change has also been observed compared with conventional stainless steel. The interfaces provided by the sub-grain boundaries and nano-oxide inclusions act as effective trap sites for helium bubbles, which contributed to the enhancement of helium tolerance.

1. Introduction

Additive manufacturing (AM), commonly known as three-dimensional (3D) printing, is a near-net shape technology, which fabricates materials based on a layer-by-layer manufacturing according to 3D digital model data. Since AM technology changes the ways to fabricate the complex components used in the nuclear reactors, and significantly reduces the economic costs and production cycle, it has attracted much attention from both the nuclear industries and academic researchers [1–3]. Selective laser melting (SLM) is one of the most promising AM technology for metals and alloys. A series of important progresses, such as the joining of Inconel 718 with 316L SS and ITER In-Vessel components, have been made in the research of AM technology for fission or fusion reactors related materials and components [4–8].

Austenitic 316L stainless steel (316L SS) has been extensively used as the components in nuclear power plants owing to its good mechanical properties, corrosion and oxidation resistance, and formability [9–12]. However, after long-term exposure in the radiation condition of fission or fusion reactors, 316L SS will generate large amount of radiation defects and helium (He) atoms, which leads to He bubbles, swelling, and radiation hardening, affecting the physical and mechanical properties of materials [13–17]. In recent years, the special microstructure containing cellular sub-grains and nano-inclusions has been reported in SLM 316L SS. The variations in microstructures between the SLM 316L SS and the steel prepared by traditional process will not only cause the changes in the mechanical properties and corrosion resistance [18–23], but also may have unexpected effects on its radiation resistance. Hence, no matter from the aspect of evaluating the performance of a novel promising material used in the nuclear reactors, or on the purpose of understanding the interactions between the special microstructures in materials and the radiation defects, it is of great significance to explore the behaviors of SLM fabricated 316L SS under the extreme radiation environment.

In this study, we presented the internal effects of microstructure on bubbles distribution and hardness of SLM 316L SS, which was irradiated by He ions at 450 °C. Transmission electron microscopy (TEM) and Nanoindentation tests were performed to examine the microstructure and harness of pre- and post- irradiated samples, respectively. The influence of microstructure on the density of bubbles and swelling rate was discussed in detail.

* Corresponding author at: Department of Nuclear Science & Engineering, Nanjing University of Aeronautics and Astronautics, Nanjing 211106, China.
E-mail address: tangxiaobin@nuaa.edu.cn (X. Tang).

https://doi.org/10.1016/j.apsusc.2018.10.268
Received 10 May 2018; Received in revised form 25 September 2018; Accepted 30 October 2018
Available online 31 October 2018
0169-4332/

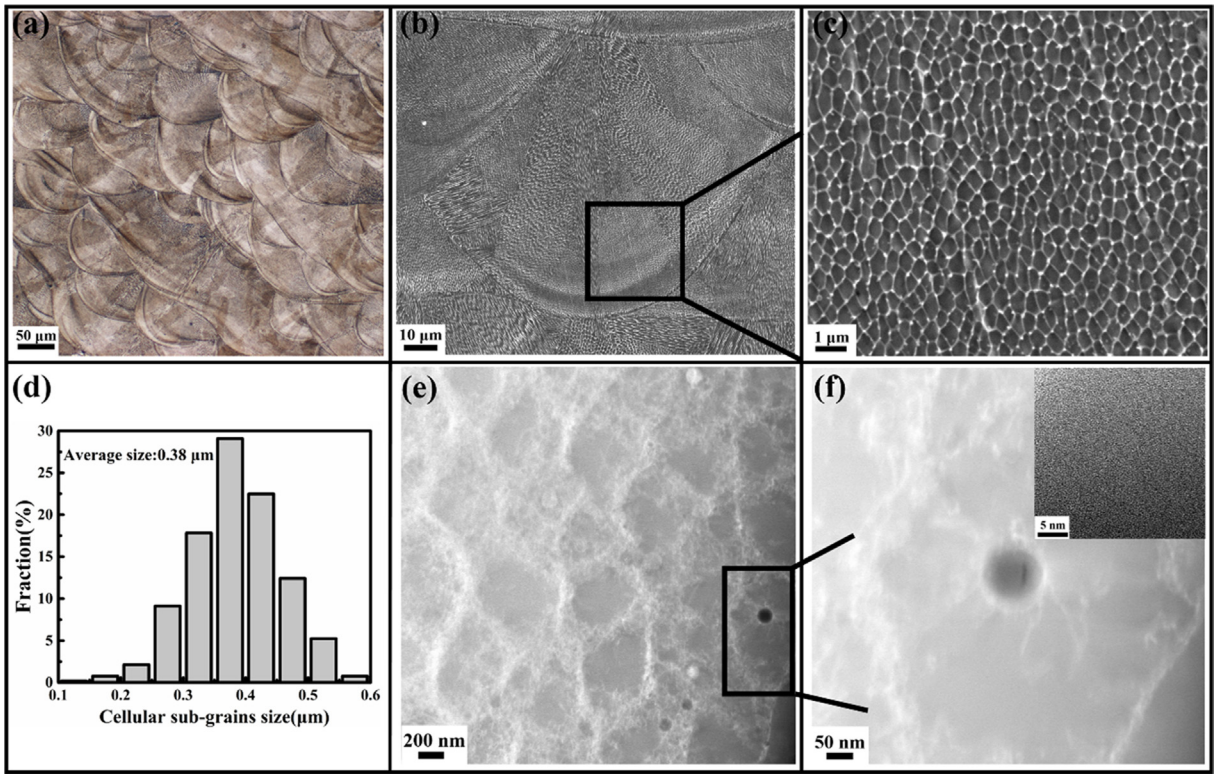

Fig. 1. Special microstructure of 316L SS fabricated by Selective Laser Melting. (a) Optical micrographs of melt pools. (b) A SEM image, revealing melt pools, and a large percent of cellular sub-grains. (c) An enlarged SEM image of cellular sub-grains. (d) The size of cellular sub-grains distribution in region (c). (e) A scanning TEM (STEM) image of cellular sub-grains and nano inclusions. (f) An enlarged STEM image of nano inclusions. The inset is a high resolution TEM image of the inclusion.

2. Experimental

2.1. Materials and He ions irradiation

In this work, the samples were generated using a selective laser melting facility BLT-S300 (Xi'an Bright Laser Technologies Co. China), equipped with an IPG fiber laser with maximum 500 W power output and 70 μm diameter laser spot. In the building process, the fixed laser parameters (power of 200 W, scan speed of 850 mm/s and line spacing of 0.1 mm) were used to obtain the highest density samples. The specimens with size $50 \times 30 \times 30\,mm^3$ were prepared in argon atmosphere and cooled inside the furnace to room temperature. The samples were divided into two groups. Each group adopted a specific approach for post-processing. The first group were bulk samples, which were irradiated by 500 keV He ions with the fluence of $1.5 \times 10^{16}\,cm^{-2}$ performed on the 320 kV platform at the Institute of Modern Physics, Chinese Academy of Sciences (CAS). Since most commercial reactors work in a temperature ranging between 200 and 550 °C, the radiation tolerance performance data of 316L SS in this temperature range is the most abundant, especially at 450 °C [24–26]. The irradiation experiments were performed at 450 °C. The depth profile of atoms distribution and damage events calculated using SRIM2013 [27] were shown in Fig. S1(a). And the irradiation depth induced by 500 keV He-ions can meet the requirements of experimental characterizations for the bulk specimens. In a second approach, we conducted a more convincing experiment to observe the microstructure evolution before and after He ions irradiation in a same TEM foil, at the same He-ions concentration with the first group. From the experiments, more contrastive results can be achieved. And the implantation experiments were then performed on the Accelerator Laboratory of Wuhan University, using 12 keV He ions with the fluence of $0.5 \times 10^{16}\,cm^{-2}$ at 450 °C. Fig. S1(b) shows the depth profile of atoms distribution and damage events.

2.2. Characterization

The microstructure of the first group of SLM 316L samples were characterized by multi-scale methods including X-ray diffraction (XRD, D8 Advance), optical microscopy (OM, Zeiss Scope A1), scanning electron microscope (SEM, Apollo 300), and transmission electron microscope (TEM, Tecnai G2 F20 S-Twin). To identify the crystal structure of the pre- and post-irradiated SLM samples, grazing incidence X-ray diffraction (GIXRD) with a CuKα (λ = 1.54 Å) target was used with the incident angle fixed at 1°. Samples for OM and SEM observation were ground by SiC papers and mechanically polished using diamond suspensions to obtain a mirror surface, then they were etched using Ralph's solution. TEM foils for pre-irradiated specimens were prepared by a standard double-jet procedure (MTPA-5, Shanghai Jiaotong University). Another cross section TEM specimens were prepared via focused ion beam (FIB, FEI Helios Nanolab 600) milling to better reflect the distribution of bubbles with depth for bulk specimens. Nanoindentation tests (Nano Indenter G200, Agilent) for the bulk samples before and after irradiation were performed using a continuous stiffness measurement method with a Berkovich-type indenter [28,29]. The maximum indentation depth was set at 1250 nm. The hardness value was identified from five indentation tests for each sample.

3. Results and discussion

The ripple-like melt pools with sizes varying from 50 to 200 μm in the etched samples observed by OM are shown in Fig. 1(a), which formed along the laser scanning track because of the high temperature of focal spot heated momentarily above the melting temperature of 316L SS powder. Suryawanshi and Ahmadi et al. also observed ripple-like melt pools in the 316L SS samples which fabricated by SLM process with different laser parameter [30,31]. In addition, cellular sub-grains also exist with an average size of 380 nm, decorated with high density

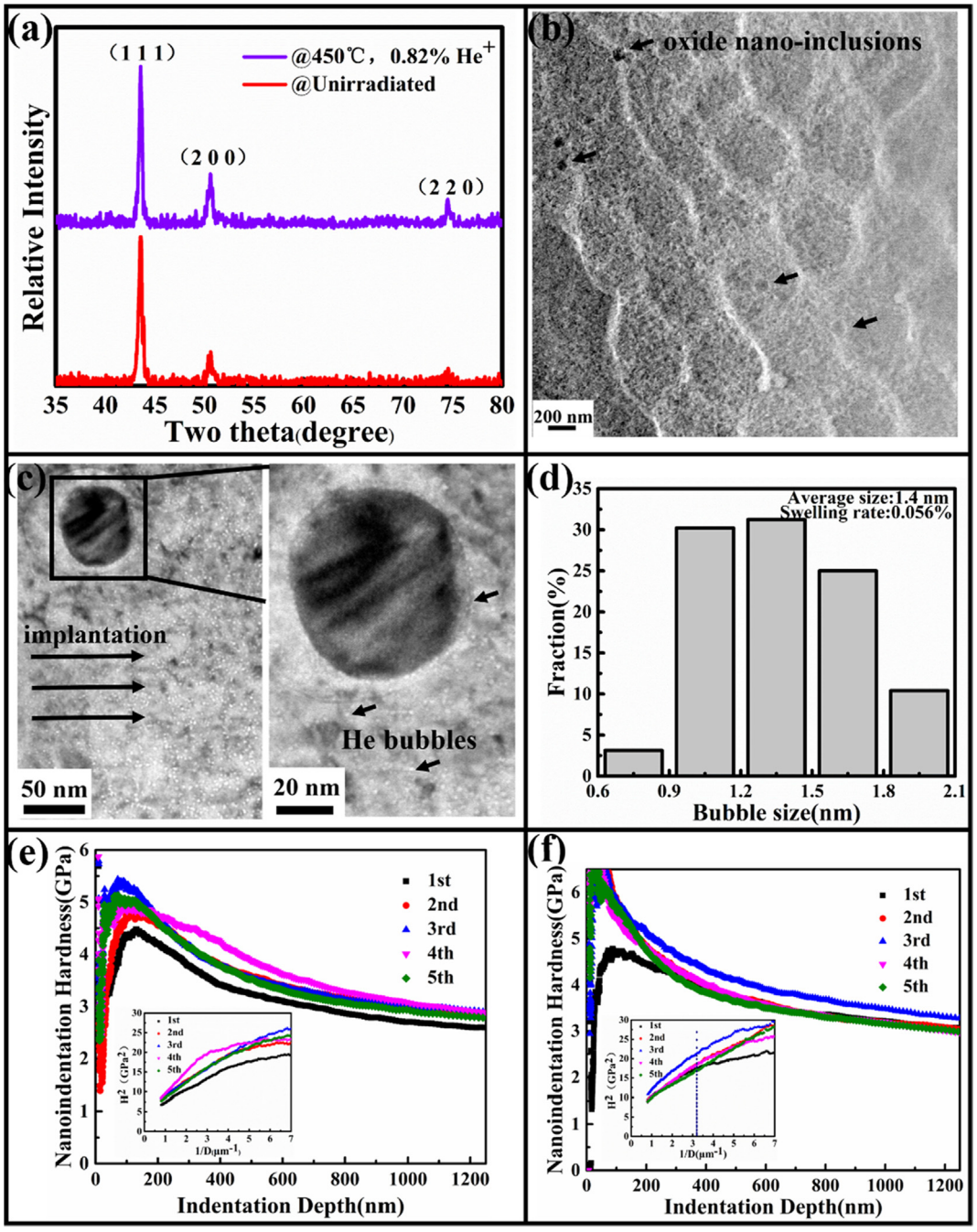

Fig. 2. The microstructure of post-irradiated bulk samples and the changing of hardness. (a) GIXRD spectra obtained on a SLM 316L SS before and after irradiation. (b) A STEM image, revealing the cellular sub-grains and nano inclusions in post-irradiated samples. (c) A bright field TEM micrograph showing the distribution of He bubbles. The right one shows a smaller density of He bubbles distributing around the surface of the nano inclusion. (d) Size distribution of bubbles. (e) and (f) The nanoindentation hardness versus the indentation depth of pre- and post-irradiated specimens, respectively. The insets show curves of $H^2 - 1/D$ for pre- and post-irradiated specimens. And the dotted vertical line in the inset of (f) was used for identifying the bi-linearity.

dislocations (Fig. 1(b–e)). The size of cellular structures observed here in the SLM 316L SS are much smaller than what have been observed in welded steels under a rapid cooling condition, typically with size between 10 and 20 μm [19]. Sun and Liu et al. reported the same microstructures surrounded with dense dislocations in a low porosity SLM 316L SS. And the size of cellular structure could be effectively adjusted to 200–1000 nm using different scanning speeds with the line spacing of 100 μm and the power output of 100 W. One possible explanation for the formation of cellular structure is that the high thermal gradient and the high solidification rate appeared in the fabrication process [32–34]. In addition, a large amount of spherical nano-size inclusions are also observed under TEM. The average size and number density of inclusions obtained by image analysis were measured approximately 60 nm and $4.2 \times 10^{20}\,m^{-3}$, respectively. And the amount of inclusions obtained was approximately 5 vol%. A high resolution TEM image with the inserted selected area electron diffraction (SAED) pattern (See Fig. S3) shows that the nanoparticles are amorphous. The EDS linear scanning was used to analysis the compositions of the spherical inclusion, which further confirms that the inclusion contains Si, Cr, O, and Mn. And the result is agreement with Sun's work [34], which used a fast scanning speeds to prepare a low porosity 316L SS parts via SLM process. The oxygen content in the facility and a high cooling rate in the

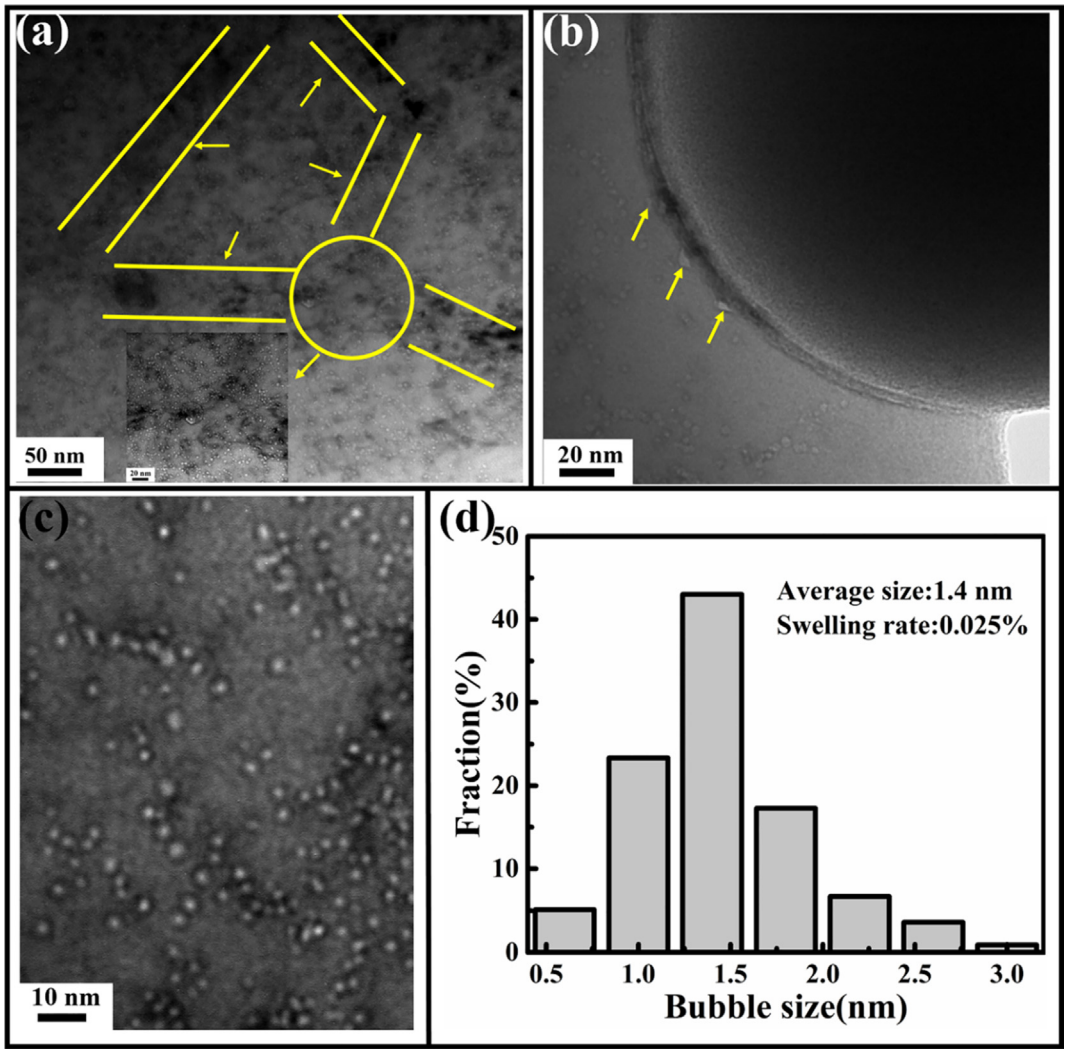

Fig. 3. Microstructure of post-irradiated TEM thin samples. (a) A TEM image, showing the He bubbles distribution near the SGBs. The yellow lines represent the SGBs formed in the SLM fabrication process. The yellow circles indicate the area around the boundary of three SGBs, and the inset shows the bubbles distribution of this area with a higher magnification TEM image. (b) The distribution of He bubbles near the interface between the inclusion and matrix. (c) and (d) A higher magnification TEM image of He bubbles and the size distribution of bubbles. (For interpretation of the references to colour in this figure legend, the reader is referred to the web version of this article.)

SLM process may be the key factor in the formation of nano-size inclusions.

Compared with the microstructure before and after irradiation, the samples remained original FCC phase without the formation of detectable second phase (Fig. 2(a)). Fig. 2(b) and (c) show the cross-sectional TEM specimen of bulk samples, which were thinned to 80 nm via FIB. The cellular sub-grains and nano inclusions can still be observed in post-irradiated samples, and their morphology and size do not obviously change compared with Fig. 1(e). A large amount of He bubbles formed in the highest He-atoms concentration region, namely, the depth around 900–1050 nm, as shown in Fig. 2(c). The average size and density of He bubbles are 1.4 nm and $3.6 \times 10^{23}\,m^{-3}$, respectively. Owing to the accumulation of He bubbles, materials swelling rate induced by the irradiation was deduced to be 0.056%, which was calculated as their volume fraction [35]. Compared with previous reports of traditional 316L SS within the same concentration of He atoms around 0.8% [25,26], which was irradiated by 10 keV He ions at 450 °C, the size of bubbles is almost unchanged. However, the density of He bubbles and the swelling rate are reduced especially compared with 316L SS prepared by traditional process [25]. The comparison details were shown in Table S1. The difference in process between SLM and traditional methods leads to the variations in microstructures. In present report, cellular sub-grains and nano inclusions were stable in the pre- and post-irradiated SLM 316L SS samples, which increases the fraction of interfaces compared with conventional samples. And this may play a key role in the mobility of He atoms and irradiated defects. A more detailed discussion will be presented later in the article.

Fig. 2(e) and (f) show the average nano-indentation hardness of SLM 316L SS before and after irradiation as a function of the indentation depth. To get rid of the indentation size effect, the hardness data were plotted as the square of hardness (H^2) versus the reciprocal of indentation depth ($1/D$) according to the report of Kasada et al. [36,37], as shown in the inserted picture. For original samples, the curve shows a good linearity when the indentation depth is greater than 140 nm. However, a bi-linearity with an indentation depth around 285–333 nm appears in the curve for post-irradiated samples. Removing the data that are significantly different from other results of the five tests, the hardness of pre- and post-irradiated bulk specimens were calculated as 2.6 GPa and 3.1 GPa, respectively. It is obvious that the hardness increased about 19% to original specimens. Hunn et al. also found a similar hardening effect in the study of 316LN SS fabricated by conventional process, which was irradiated by He ions at 200 °C [38]. And the enhancement of hardness increases from 25% to 48%, when the concentration increases from 0.22% to 1%. The table of comparing

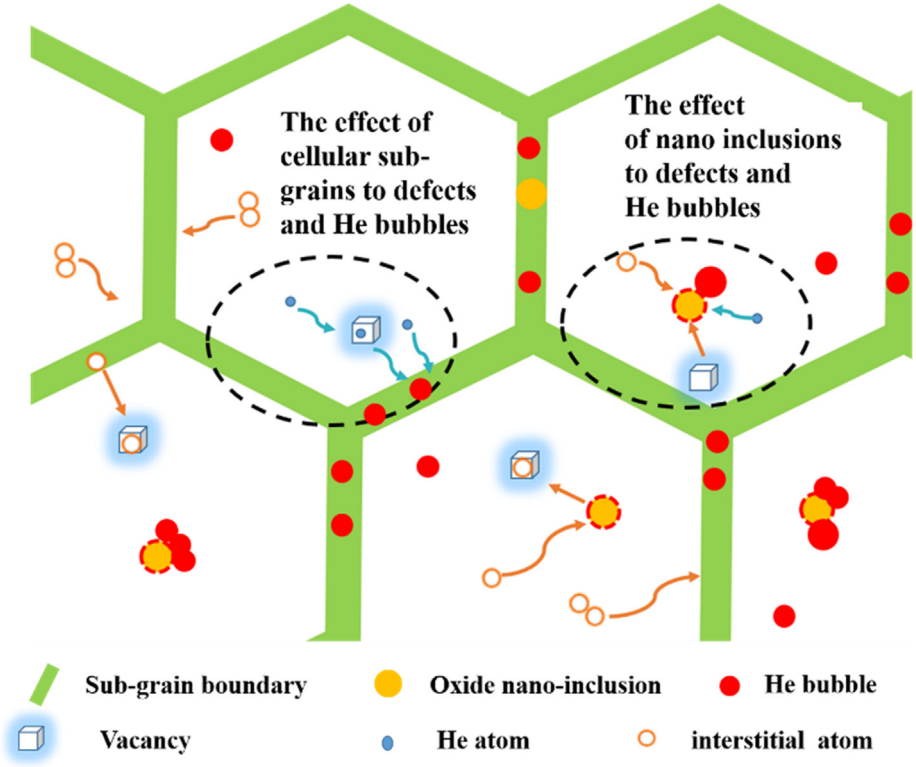

Fig. 4. Schematic diagram of the effects of SGBs and inclusions to radiation defects and He bubbles (not to scale).

percent hardening between the SLM 316L SS with previous work was added in the Supplementary material Table S2. It is obvious that the percent hardening of Hunn's work is larger than our work, even though under a low concentration of He ions. Contributed to the Friedel-Kroupa-Hirsch (FKH) relation, the larger the cavity size and/or cavity density for a given material, the higher ΔH is [39]. According to the result of TEM images, the density of bubbles is lower than the conventional samples [25,26]. We think the sub-grains and nano inclusions formed in the fabrication process increase the fraction of interfaces, which influence the bubbles size and density. And this may be the key factor for a lower hardness enhancement compared with the Ref. [38].

In order to narrow the observation region, get more contrastive results from the microstructure and the distribution of He bubbles before and after irradiation, we carried out another irradiation experiment on the same TEM thin samples, and the details are shown in Fig. S1(b). The results of Figs. S2(a) and (b) are similar to those of Fig. 2(b) and (c), indicating the stability of the cellular sub-grains and nano-inclusions under this irradiation condition. As shown in Fig. 3(a), He bubbles were observed both in the matrix and sub-grain boundaries (SGBs). However, the density of He bubbles did increase at SGBs. A larger size about 3 nm of He bubbles was observed around the nano-inclusions, with a smaller density of He bubbles (Fig. 3(b)). The size of He bubbles is shown in Fig. 3(c) and (d), and a detail comparison between this study and previous works is shown in the Supplementary material Table S1. In the Ref. [25], the irradiation experiment was performed with a concentration around 0.83% at 450 °C for conventional 316L SS. And the size of bubbles was 1.6 nm, which is similar with our work. Although the only two irradiation experiments cannot show the detail comparison of bubble size and density between SLM 316L SS and conventional 316L SS, it can be seen roughly from Table S1 that the bubble density and swelling rate of post-irradiated samples in this work is lower than the Ref. [25] with a concentration around 0.83% at 450 °C.

The mobility of He atoms is limited by the strength and density of trap sites [40]. Previous works [41–43] have proved that grain boundaries (GBs) can act as preferential trap sites for irradiation-induced defects and He atoms due to the low migration energy of interstitial He atoms allowing them to move quickly to GBs. In present report, cellular sub-grains were stable in the pre- and post-irradiated samples. And a larger density of bubbles appeared to be in immediate the SGBs (Fig. 3(a)), suggesting that the SGBs are highly effective He trapping sites like GBs. As shown in Fig. 4, compared with other conventional 316L SS with coarse grains, cellular sub-grains increase the fraction of interfaces in material. And interstitial atoms recombine with the vacancies when they migrate to the SGBs, reducing the probability of He-vacancy complex formation, which eventually weak the bubble nucleation and growth. The region in Fig. 2(c) contains a 40–60 nm nano-inclusion. He bubbles, obviously like white circles, seem to be in contact with the interface between nano-inclusion and matrix. And some the bubbles surround the nano-inclusions, which is larger than those in other regions (Fig. 3(b)), indicating that the nano-inclusions are preferential absorption and growth sites for He [40,44]. The nano-inclusion also provide more interfaces, acting as recombine sites for interstitial atoms and vacancies, which affects the diffusion of He atoms and the nucleation of bubbles. Thus, SLM 316L SS has a good He tolerance, with a much smaller density of bubbles and swelling rate of material than those 316L SS fabrication by conventional process.

As we all know, the enhancement in hardness (ΔH), is mainly related to the bubbles or voids. Contributed to the Friedel-Kroupa-Hirsch (FKH) relation, the larger the cavity size and/or cavity density for a given material, the higher ΔH is [39]. Compared with Ref. [38], a high temperature in present work helps bubbles nucleation, which influence the ΔH. It can be seen roughly from Table S2 that the percent hardening in this work is lower than the Ref. [38], with a low concentration from 0.22% to 0.52%. The value of percent hardening in the Ref. [38] is approximately two times as much in our work with the concentration of 0.52%. And it is mainly related to a large fraction of interfaces in the SLM 316L SS, which provides more excellent sinks for defects and He atoms, reducing the density of He bubbles, thus the enhancement of hardness decreased.

4. Conclusion

In summary, structural and mechanical properties of 316L SS fabricated by SLM subjected to He-ions irradiation at 450 °C with the concentration approximately 0.8% were investigated by SEM, TEM, and nanoindentation. The results show that SLM 316L SS has great He radiation tolerance in the condition of our work. There are a considerable number of cellular sub-grains and nano-inclusions distributed in SLM 316L SS before and after the radiation conditions, increasing the volume fraction of interfaces, which serve as effective sinks for He atoms and radiation defects, reducing the density of He bubbles, the swelling rate of material and the enhancement in hardness. It is worth noting that the presently work has specifically revealed the internal effects of microstructure on bubbles and hardness of SLM 316L SS, which was irradiated by He ions at 450 °C. Further parameter developments for studying irradiation effects details like temperatures, energies and fluences are needed. Comparison of irradiation behavior of SLM and traditional 316L SS need to be clarified in future work on this topic.

Acknowledgement

This work was supported by the National Natural Science Foundation of China (Grant No. 11705087), the Natural Science Foundation of Jiangsu Province (Grant No. BK20170776), and the Foundation of Graduate Innovation Center in NUAA (Grant No. kfjj20170609). The irradiation experiments were performed on the 320 kV platform at the Institute of Modern Physics, CAS and the Accelerator Laboratory of Wuhan University. We thank the help of Tongmin Zhang, Long Kang, Jinyu Li, Huiping Liu, and Weiping Zhang during the ion irradiation experiments. Thanks to the Suzhou Institute of Nano-Tech and Nano-Bionics, CAS for the support of Nanoindentation tests.

Appendix A. Supplementary material

Supplementary data to this article can be found online at https://doi.org/10.1016/j.apsusc.2018.10.268.

References

[1] Y. Zhong, L.E. Rännar, S. Wikman, A. Koptyug, L. Liu, D. Cui, Z. Shen, Additive manufacturing of ITER first wall panel parts by two approaches: selective laser melting and electron beam melting, Fusion Eng. Des. 116 (2017) 24–33.
[2] M.L. Pace, A. Guarnaccio, P. Dolce, D. Mollica, G.P. Parisi, A. Lettino, L. Medici, V. Summa, R. Ciancio, A. Santagata, 3D additive manufactured 316L components microstructural features and changes induced by working life cycles, Appl. Surf. Sci. 418 (2017) 437–445.
[3] A. Röttger, K. Geenen, M. Windmann, F. Binner, W. Theisen, Comparison of microstructure and mechanical properties of 316 L austenitic steel processed by selective laser melting with hot-isostatic pressed and cast material, Mater. Sci. Eng. A 678 (2016) 365–376.
[4] A. Hinojos, J. Mireles, A. Reichardt, P. Frigola, P. Hosemann, L.E. Murr, R.B. Wicker, Joining of inconel 718 and 316 stainless steel using electron beam melting additive manufacturing technology, Mater. Des. 94 (2016) 17–27.
[5] D. Herzog, V. Seyda, E. Wycisk, C. Emmelmann, Additive manufacturing of metals, Acta Mater. 117 (2016) 371–392.
[6] B. Huang, Y. Zhai, S. Liu, X. Mao, Microstructure anisotropy and its effect on mechanical properties of reduced activation ferritic/martensitic steel fabricated by selective laser melting, J. Nucl. Mater. 500 (2018) 33–41.
[7] Y. Zhong, L. Liu, S. Wikman, D. Cui, Z. Shen, Intragranular cellular segregation network structure strengthening 316L stainless steel prepared by selective laser melting, J. Nucl. Mater. 470 (2016) 170–178.
[8] X. Zhou, X. Liu, D. Zhang, Z. Shen, W. Liu, Balling phenomena in selective laser melted tungsten, J. Mater. Process. Technol. 222 (2015) 33–42.
[9] S. Şahin, M. Übeyli, A review on the potential use of austenitic stainless steels in nuclear fusion reactors, J. Fusion Energy 27 (2008) 271–277.
[10] K. Chandra, V. Kain, V.S. Raja, R. Tewari, G.K. Dey, Low temperature thermal ageing embrittlement of austenitic stainless steel welds and its electrochemical assessment, Corros. Sci. 54 (2012) 278–290.
[11] L. Zhang, J. Wang, Effect of temperature and loading mode on environmentally assisted crack growth of a forged 316L SS in oxygenated high-temperature water, Corros. Sci. 87 (2014) 278–287.
[12] X. Zhang, J. Wang, H. Fan, D. Pan, Erosion–corrosion resistance properties of 316L austenitic stainless steels after low-temperature liquid nitriding, Appl. Surf. Sci. 440 (2018) 755–762.
[13] O.K. Chopra, A.S. Rao, A review of irradiation effects on LWR core internal materials – IASCC susceptibility and crack growth rates of austenitic stainless steels, J. Nucl. Mater. 409 (2011) 235–256.
[14] V. Muthukumaran, V. Selladurai, S. Nandhakumar, M. Senthilkumar, Experimental investigation on corrosion and hardness of ion implanted AISI 316L stainless steel, Mater. Des. 31 (2010) 2813–2817.
[15] N. Sakaguchi, Y. Ohguchi, T. Shibayama, S. Watanabe, H. Kinoshita, Surface cracking on Σ3, Σ9 CSL and random grain boundaries in helium implanted 316L austenitic stainless steel, J. Nucl. Mater. 432 (2013) 23–27.
[16] W. Hu, L. Guo, J. Chen, F. Luo, T. Li, Y. Ren, Synergistic effect of helium and hydrogen for bubble swelling in reduced-activation ferritic/martensitic steel under sequential helium and hydrogen irradiation at different temperatures, Fusion Eng. Des. 89 (2014) 324–328.
[17] T. Miura, K. Fujii, K. Fukuya, Micro-mechanical investigation for effects of helium on grain boundary fracture of austenitic stainless steel, J. Nucl. Mater. 457 (2015) 279–290.
[18] E. Liverani, S. Toschi, L. Ceschini, A. Fortunato, Effect of selective laser melting (SLM) process parameters on microstructure and mechanical properties of 316L austenitic stainless steel, J. Mater. Process. Technol. 249 (2017) 255–263.
[19] K. Saeidi, X. Gao, Y. Zhong, Z.J. Shen, Hardened austenite steel with columnar sub-grain structure formed by laser melting, Mater. Sci. Eng. A 625 (2015) 221–229.
[20] X. Lou, M. Song, P.W. Emigh, M.A. Othon, P.L. Andresen, On the stress corrosion crack growth behaviour in high temperature water of 316L stainless steel made by laser powder bed fusion additive manufacturing, Corros. Sci. 128 (2017) 140–153.
[21] X. Lou, P.L. Andresen, R.B. Rebak, Oxide inclusions in laser additive manufactured stainless steel and their effects on impact toughness and stress corrosion cracking behavior, J. Nucl. Mater. 499 (2018) 182–190.
[22] D. Wang, C. Song, Y. Yang, Y. Bai, Investigation of crystal growth mechanism during selective laser melting and mechanical property characterization of 316L stainless steel parts, Mater. Des. 100 (2016) 291–299.
[23] Q. Chao, V. Cruz, S. Thomas, N. Birbilis, P. Collins, A. Taylor, P.D. Hodgson, D. Fabijanic, On the enhanced corrosion resistance of a selective laser melted austenitic stainless steel, Scr. Mater. 141 (2017) 94–98.
[24] J. Van Den Bosch, G. Coen, R.W. Bosch, A. Almazouzi, TWIN ASTIR: first tensile results of T91 and 316L steel after neutron irradiation in contact with liquid lead – bismuth eutectic, J. Nucl. Mater. 398 (2010) 68–72.
[25] S. Jublot-Leclerc, M.L. Lescoat, F. Fortuna, L. Legras, X. Li, A. Gentils, TEM study of the nucleation of bubbles induced by He implantation in 316L industrial austenitic stainless steel, J. Nucl. Mater. 466 (2015) 646–652.
[26] A. De Backer, G. Adjanor, C. Domain, M.L. Lescoat, S. Jublot-Leclerc, F. Fortuna, A. Gentils, C.J. Ortiz, A. Souidi, C.S. Becquart, Modeling of helium bubble nucleation and growth in austenitic stainless steels using an Object Kinetic Monte Carlo method, Nucl. Instrum. Meth. Phys. Res. B 352 (2015) 107–114.
[27] J.F. Ziegler, M.D. Ziegler, J.P. Biersack, SRIM – the stopping and range of ions in matter, Nucl. Instrum. Meth. Phys. Res. B 268 (2010) (2010) 1818–1823.
[28] H.F. Huang, J.J. Li, D.H. Li, R.D. Liu, G.H. Lei, Q. Huang, L. Yan, TEM, XRD and nanoindentation characterization of Xenon ion irradiation damage in austenitic stainless steels, J. Nucl. Mater. 454 (2019) 168–172.
[29] Z.Y. Fu, P.P. Liu, F.R. Wan, Q. Zhan, Helium and hydrogen irradiation induced hardening in CLAM steel, Fusion Eng. Des. 91 (2015) 73–78.
[30] A. Ahmadi, R. Mirzaeifar, N.S. Moghaddam, A.S. Turabi, H.E. Karaca, M. Elahinia, Effect of manufacturing parameters on mechanical properties of 316L stainless steel parts fabricated by selective laser melting: a computational framework, Mater. Des. 112 (2016) 328–338.
[31] J. Suryawanshi, K.G. Prashanth, U. Ramamurty, Mechanical behavior of selective laser melted 316L stainless steel, Mater. Sci. Eng. A 696 (2017) 113–121.
[32] L. Liu, Q. Ding, Y. Zhong, J. Zou, J. Wu, Y.L. Chiu, J. Li, Z. Zhang, Q. Yu, Z. Shen, Dislocation network in additive manufactured steel breaks strength-ductility trade-off, Mater. Today 21 (2018) 354–361.
[33] Y.M. Wang, T. Voisin, J.T. McKeown, J. Ye, N.P. Calta, Z. Li, Z. Zeng, Y. Zhang, W. Chen, T.T. Roehling, R.T. Ott, M.K. Santala, P.J. Depond, M.J. Matthews, A.V. Hamza, T. Zhu, Additively manufactured hierarchical stainless steels with high strength and ductility, Nat. Mater. 17 (2018) 63–70.
[34] Z. Sun, X. Tan, S.B. Tor, W.Y. Yeong, Selective laser melting of stainless steel 316L with low porosity and high build rates, Mater. Des. 104 (2016) 197–204.
[35] P.P. Liu, Q. Zhan, Z.Y. Fu, Y.P. Wei, Y.M. Wang, F.M. Wang, S. Ohnuki, F.R. Wan, Surface and internal microstructure damage of He-ion-irradiated CLAM steel studied by cross-sectional transmission electron microscopy, J. Alloys Compd. 649 (2015) 859–864.
[36] Y. Takayama, R. Kasada, Y. Sakamoto, K. Yabuuchi, A. Kimura, M. Ando, D. Hamaguchi, H. Tanigawa, Nanoindentation hardness and its extrapolation to bulk-equivalent hardness of F82H steels after single- and dual-ion beam irradiation, J. Nucl. Mater. 442 (2013) S23–S27.
[37] X. Zhang, X. Mei, X. Cao, Y. Wang, J. Sun, The effect of He ions irradiation on the microstructure and property of CLF-1 steel, J. Nucl. Mater. 509 (2018) 496–503.
[38] J.D. Hunn, E.H. Lee, T.S. Byun, L.K. Mansur, Helium and hydrogen induced hardening in 316LN stainless steel, J. Nucl. Mater. 282 (2000) 131–136.
[39] L.X. Yang, S.J. Zheng, Y.T. Zhou, J. Zhang, Y.Q. Wang, C.B. Jiang, N.A. Mara, I.J. Beyerlein, X.L. Ma, Effects of He radiation on cavity distribution and hardness of bulk nanolayered Cu-Nb composites, J. Nucl. Mater. 487 (2017) 311–316.
[40] P.D. Edmondson, C.M. Parish, Y. Zhang, A. Hallén, M.K. Miller, Helium entrapment in a nanostructured ferritic alloy, Scr. Mater. 65 (2011) 731–734.
[41] F. Chen, X. Tang, H. Huang, X. Li, Y. Wang, C. Huang, J. Liu, H. Li, D. Chen, Formation of He-rich layers observed by neutron reflectometry in the He-ion-irradiated Cr/W multilayers: effects of Cr/W interfaces on the He-trapping behavior, ACS Appl. Mater. Interfaces 8 (2016) 24300–24305.
[42] H. Huang, X. Tang, F. Chen, J. Liu, D. Chen, Role of graphene layers on the radiation resistance of copper–graphene nanocomposite: inhibiting the expansion of thermal spike, J. Nucl. Mater. 493 (2017) 322–329.
[43] O. El-Atwani, J.E. Nathaniel, A.C. Leff, B.R. Muntifering, J.K. Baldwin, K. Hattar, M.L. Taheri, The role of grain size in He bubble formation: implications for swelling resistance, J. Nucl. Mater. 484 (2017) 236–244.
[44] Q. Li, C.M. Parish, K.A. Powers, M.K. Miller, Helium solubility and bubble formation in a nanostructured ferritic alloy, J. Nucl. Mater. 445 (2014) 165–174.